Nano Research 2017, 10(1): 187–198
DOI 10.1007/s12274-016-1277-5
Research Article
ISSN 1998-0124
CN 11-5974/O4

Layer-controlled Pt-Ni porous nanobowls with enhanced electrocatalytic performance

Hongsheng Fan[1], Ming Cheng[1], Zhenlei Wang[1], and Rongming Wang[2] (✉)

[1] *Department of Physics, Beihang University, Beijing 100191, China*
[2] *School of Mathematics and Physics, University of Science and Technology Beijing, Beijing 100083, China*

Received: 8 July 2016
Revised: 21 August 2016
Accepted: 2 September 2016

KEYWORDS
Pt-Ni nanobowls,
facile synthesis,
sodium citrate,
poly(vinylpyrrolidone) (PVP),
electrocatalysis

ABSTRACT

Hollow and porous Pt-based nanomaterials are promising catalysts with applications in many sustainable energy technologies such as fuel cells. Economical and green synthetic routes are highly desirable. Here, we report a facile approach to prepare double- and single-layered Pt-Ni nanobowls (DLNBs and SLNBs) with porous shells. Microstructural analysis revealed that the shells were constructed of alloyed Pt-Ni nanocrystals and small amounts of Ni compounds. X-ray photoelectron spectra showed that their Pt 4f binding energies shifted in the negative direction compared to those of the commercial Pt/C catalyst. Furthermore, the DLNBs contained greater contents of oxidized Ni species than the SLNBs. The layer-controlled growth processes were confirmed by microscopy, and a formation mechanism was proposed based on the assistance of citrate and poly(vinylpyrrolidone) (PVP). For the methanol oxidation reaction, the DLNBs and SLNBs exhibited 2.9 and 2.5 times higher mass activities than that of the commercial Pt/C catalyst, respectively. The activity enhancements were attributed to electronic effects and a bifunctional mechanism. Chronoamperometry and prolonged cyclic voltammetry indicated that the Pt-Ni bowl-like structures had better electrochemical properties and structural stability than the commercial Pt/C catalyst, thus making the Pt-Ni nanobowls excellent electrocatalysts for use in direct methanol fuel cells.

1 Introduction

Platinum (Pt) based nanomaterials are key catalytic components in many promising industrial and commercial devices because of their excellent ability to promote oxidation and reduction processes [1]. Because of the rarity and cost of platinum, catalytic activity often increased by increasing the specific surface area or atomic catalytic activity [2, 3]. Small Pt nanoparticles loaded on various supports (e.g., carbon materials and metal oxides) show increased surface-to-volume ratios but can suffer from problems

Address correspondence to rmwang@ustb.edu.cn

introduced by the supports, such as corrosion and structural collapse of the support during reaction [4, 5]. Constructing three-dimensional architectures increases the specific surface area considerably and can lead to greater structural and catalytic stability [6–9]. Alternatively, Pt can be combined with other elements at the nanoscale to form alloy, segregation or core–shell architectures [10]. Benefiting from the electronic effects and bifunctional mechanism of the integrated components, the specific catalytic activity and poison tolerance of the multi-component structures can be improved by adjusting the atomic arrangement and electronic structure of the catalyst [11, 12].

In the past few years, hollow Pt-based nanostructures have attracted considerable attention due to their favorable characteristics, such as high specific surface area, excellent permeability, and good stability [13–16]. As reported previously [17], the nanocage effect endows the inner surfaces of hollow structures with excellent reactivity for heterogeneous catalytic reactions, and the template-assisted method is often used to achieve these hollow structures. About ten years ago, spherical Pt nanocages were successfully assembled from dendritic nanocrystals based on either liposomes or polystyrene beads containing photocatalyst molecules [15, 18]. Furthermore, porous Pt-based nanotubes were produced using pre-made anodic aluminum oxide or tellurium rods [19, 20]. However, these strategies used soft or hard templates, which require relatively complicated preliminary or post-synthesis processes. Recently, a convenient route has been developed to solve this problem using sacrificial templates and galvanic replacement reactions, and a series of Pt-based hollow structures have been synthesized, including porous nanotubes, nanocages, and nanoframes [14, 21–24]. In addition, a dealloying process has also been employed to generate Pt-based nanoframes using alloyed nanocrystals as precursors [13, 25, 26].

Despite this progress, these catalysts are still far from practical use, mainly because these high-performance catalysts are usually prepared in organic solution or by heating, processes that are neither cost-effective nor environmentally friendly. In recent years, Pt-M (M = Ni, Co, Fe, etc.) bimetallic nanoparticles with hollow interiors have been reported frequently, and these are prepared in aqueous solutions and at ambient temperature [27–32]. For catalytic applications, bowl-like morphologies or open structures are of interest to researchers for their optimized packing densities and unique structural features [13, 33]. However, for Pt-based materials, generation of these morphologies has been limited because achieving synthetic control is difficult. Herein, a simple method is proposed to achieve porous Pt-Ni bowls with double and single layers by utilizing sodium citrate and poly(vinylpyrrolidone) (PVP) as structure-modifying agents under mild synthetic conditions. A detailed investigation was conducted to investigate the microstructural features, electronic structure, and the formation mechanism of the nanobowls. In addition, the methanol oxidation reaction (MOR) was used as a model reaction to evaluate the catalytic performance of the Pt-Ni nanobowls.

2 Experimental

Potassium chloroplatinate (K_2PtCl_6), nickel chloride hexahydrate ($NiCl_2{\cdot}6H_2O$), sodium borohydride ($NaBH_4$), sodium citrate ($C_6H_5Na_3O_7{\cdot}2H_2O$), and PVP ($M_W$ = 30,000) were purchased from Chinese reagent companies. The commercial Pt/C catalyst (40 wt.% Pt) was purchased from Alfa Aesar. All reagents were analytical grade and used as received.

To synthesize the double-layered Pt-Ni nanobowls (Pt-Ni DLNBs), $NiCl_2{\cdot}6H_2O$ (10 mg), $C_6H_5Na_3O_7{\cdot}2H_2O$ (5 mg), and PVP (50 mg) were dissolved in high-purity water (40 mL). Then, a freshly prepared solution of $NaBH_4$ (4 mg in 2 mL water) was added quickly with vigorous magnetic stirring (about 600 rpm). After the color changed from transparent to grey, an aqueous solution of K_2PtCl_6 (2 mL, 10 mM) was added dropwise. The resultant black solution was stirred for another 2 h, and the product was collected by centrifugation and washed several times with water and ethanol. The single-layered Pt-Ni nanobowls (Pt-Ni SLNBs) were obtained employing the same process but with 15 mg of $C_6H_5Na_3O_7{\cdot}2H_2O$ and 5 mg of PVP.

The morphologies and structures were characterized by scanning electron microscopy (SEM; Hitachi S-4800), transmission electron microscopy (TEM; JEOL JEM-2100F at 200 kV, and FEI Titan G^2 80-300 ST at 300 kV), and X-ray diffraction (XRD; Rigaku Ultima IV, Cu Kα,

0.154 nm). Elemental composition data were determined using an energy-dispersive X-ray spectroscope (EDAX) fitted within the JEM-2100F TEM. X-ray photoelectron spectroscopy (XPS) spectra were recorded by an ESCALAB 250 system (Thermofisher) using AI Kα radiation.

The electrochemical measurements were carried out with a CHI660D electrochemical workstation (CH Instruments) at 20 ± 1 ℃. A glassy carbon disk (ϕ = 3 mm), a platinum wire and a saturated calomel electrode (SCE) were used as the working, counter, and reference electrodes, respectively. To prepare the working electrode, the Pt-based catalysts were dispersed ultrasonically in ethanol at a concentration of 0.566 $mg_{metal}\cdot mL^{-1}$, and the suspension (2.5 μL) was pipetted onto the glassy carbon substrate with a catalyst loading of about 20 $\mu g_{metal}\cdot cm^{-2}$. After drying in air, a Nafion (2.5 μL, 5 wt.%) solution was used to cover the surface of the catalyst electrode. Electrocatalytic oxidation measurements were carried out in an aqueous H_2SO_4 solution (0.5 M) and methanol (1 M), while electrochemical active surface area (ECSA) measurements were conducted in H_2SO_4 solution (0.5 M), both at a sweep rate of 50 $mV\cdot s^{-1}$.

3 Results and discussion

3.1 Morphological and structural characterization

The as-synthesized Pt-Ni DNLBs and SLNBs were first characterized by SEM, and typical images are shown in Fig. 1. In virtue of the excellent depth of field possible in SEM imaging, the bowl-like structures were easily identified with good stereo perception for both samples. A magnified SEM image is shown in Fig. 1(b), and this image shows the hollow interior with dark contrast and the double-layered feature of a single DLNB. Figure 1(c) shows two nanobowls close to each other, confirming the concave surface and the unique packing mode. The magnified SEM images in Figs. 1(e) and 1(f) show the vertical and side views of the Pt-Ni SLNBs, respectively, which reveal that the particles are single-layered and assembled of nanoparticles. The average sizes of the Pt-Ni DLNBs and SLNBs are about 256 and 214 nm, respectively, based on the statistical results of 300 nanobowls.

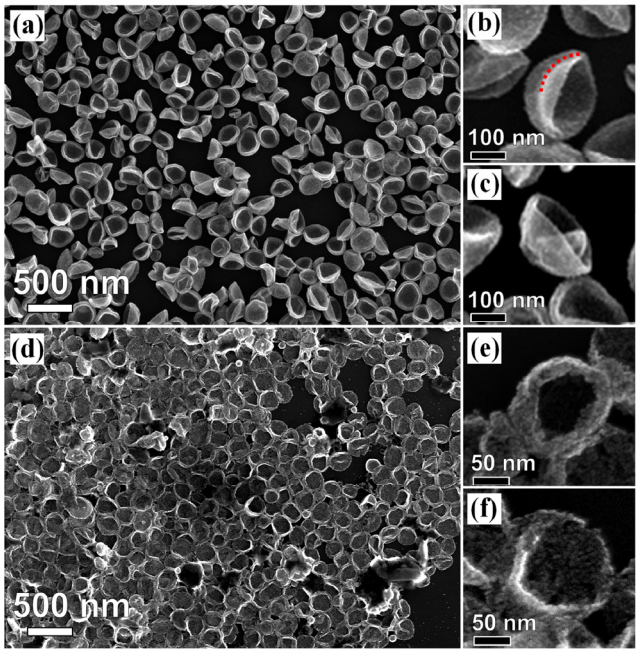

Figure 1 Typical SEM images of ((a)–(c)) Pt-Ni DLNBs and ((d)–(f)) Pt-Ni SLNBs. The red dotted line in (b) shows the outline of the concave surface of the Pt-Ni DLNBs.

The energy dispersive X-ray spectroscopy (EDS) results are shown in Fig. S1 (in the Electronic Supplementary Material (ESM)), and these demonstrate the coexistence of Pt and Ni with average composition ratios (Pt:Ni) of 76:24 and 77:23 for the DLNBs and SLNBs, respectively. Because no Cu-based precursors were added, the strong signal of Cu was ascribed to the copper sample grids.

More detailed structural characterization was carried out using analytical TEM techniques. Figures 2(a) and 2(c) show typical low-magnification TEM images of a DLNB and a SLNB, respectively. The inset images are their corresponding selected area electron diffraction (SAED) patterns, and both structures are polycrystalline face-centered cubic (fcc). For the double-layered structure, densely packed nanoparticles can be clearly distinguished by the dark contrast seen in Fig. 2(a). However, the shell was not seamless, which can be confirmed by the observation of a pore, which is indicated in the lattice-resolved high-resolution transmission electron microscopy (HRTEM) image (Fig. 2(b)). In contrast, the structure of the SLNBs was different, being more network-like and constructed of interconnected nanoparticles, as shown in Fig. 2(c). This SLNB structure suggests a more accessible surface.

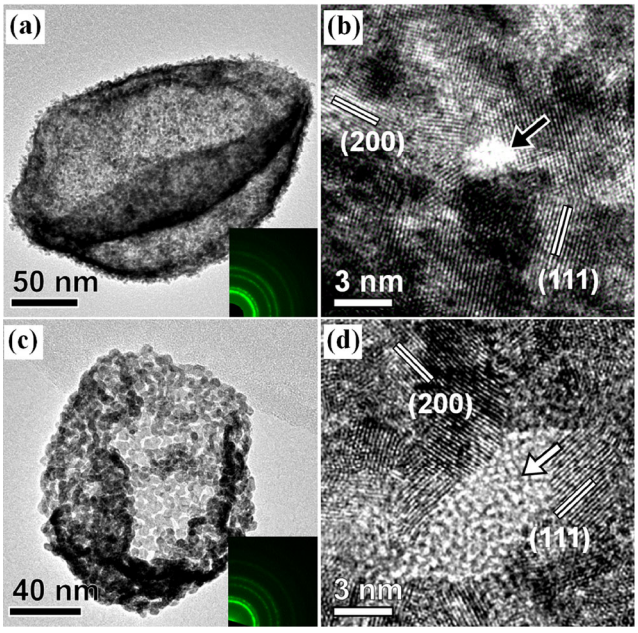

Figure 2 Low- and high-resolution TEM images of ((a) and (b)) Pt-Ni DLNBs and ((c) and (d)) Pt-Ni SLNBs. The inset images in (a) and (c) are the corresponding SAED patterns. The arrows in (b) and (d) show the pores on the surfaces.

For both samples, discrete crystalline grains of about 3 to 4 nm can be seen in the HRTEM images. In addition, the SLNB pore sizes are larger (4 nm) than those of the DLNBs (2 nm). Fringe spacings of around 2.2 and 1.9 Å for both samples correspond to the (111) and (200) planes of the fcc structure with lattice constants of about 3.8 Å. The statistical data regarding the *d*-spacings of the (111) planes were gathered by measuring 150 randomly selected nanocrystals, and the distribution curves are presented in Fig. 3(a). The average (111) spacings for DLNBs, SLNBs, and the Pt/C catalyst were calculated to be about 2.23, 2.23, and 2.28 Å, respectively. The compression of crystal lattice indicates the alloy nature of the Pt-Ni nanostructures. Assuming the composition ratio of alloyed Pt and Ni is 77:23 (or 76:24), the (111) spacing is calculated to be about 2.21 Å, smaller than the value determined from HRTEM. This indicates that some Ni atoms did not participate in the alloying processes, but instead were possibly oxidized and converted into Ni-based oxides or hydroxides. The full half-peak width (FWHM) of the *d*-spacing distribution of the Pt-Ni SLNBs was smaller than that of the Pt-Ni DLNBs, which suggests that the elemental distribution was more uniform in the SLNBs.

Figure 3(b) shows the XRD patterns of the two kinds of Pt-Ni nanobowls and of commercial Pt/C. The as-prepared samples are both well-crystallized fcc structures, and the diffraction peaks are similar to those of Pt/C. Slight shifts to higher angles in the diffraction patterns of the Pt-Ni structures indicate the compression of the Pt lattice on alloying with Ni, in accordance with the HRTEM results. No other diffraction peaks are present in the patterns, suggesting that the crystallization of Ni-based compounds did not occur. Using the Debye–Scherer formula $D = 0.89\lambda/(\beta\cdot\cos\theta_B)$, where λ is the X-ray wavelength (0.154 nm), β is the FWHM, and the θ_B is the Bragg diffraction angle, the average sizes of crystalline grains were calculated to be 3.7, 3.6, and 3.2 nm based on the FWHMs of the (111) reflection of Pt-Ni DLNBS, SLNBs and Pt/C catalyst, respectively.

The XPS results of the as-prepared samples and Pt/C catalyst are presented in Figs. 3(c) and 3(d), and Fig. S2 (in the ESM). The Pt $4f_{7/2}$ core level peak of the DLNBs and SLNBs shifted to 70.7 and 70.9 eV, respectively. These negative shifts compared to the peak of Pt/C (71.6 eV) can be attributed to the alloying of Pt with Ni, which results in partial electron transfer from Ni to Pt due to the greater electronegativity of Pt [28, 34]. The Pt^{x+} relative peak intensities of the Pt-Ni samples were lower than those of the Pt/C catalyst, revealing that the oxidation of Pt was less severe on the surface of the Pt-Ni nanobowls. Signals for boron at 187.7 and 197.7 eV were not detected in either Pt-Ni sample, as shown in Fig. S2 (in the ESM), indicating that boron compounds were not present in the final products [31]. Furthermore, the electronic structure of the Ni component was investigated by the Ni 2p spectra shown in Fig. 3(d). Peak fitting was carried out using a previously reported method [13, 35]. In addition to metallic Ni, both Pt-Ni samples contain oxidized Ni, which formed because the synthetic process was not carried out under inert conditions and Ni on the crystal surfaces was exposed to oxygen dissolved in the aqueous synthetic solution. Moreover, the Ni^{x+} relative peak intensities of the Pt-Ni DLNBs were much higher than those of the Pt-Ni SLNBs, indicating that nickel oxides or hydroxides were richer on the surface of the DLNBs, possibly because of their different structures and formation processes.

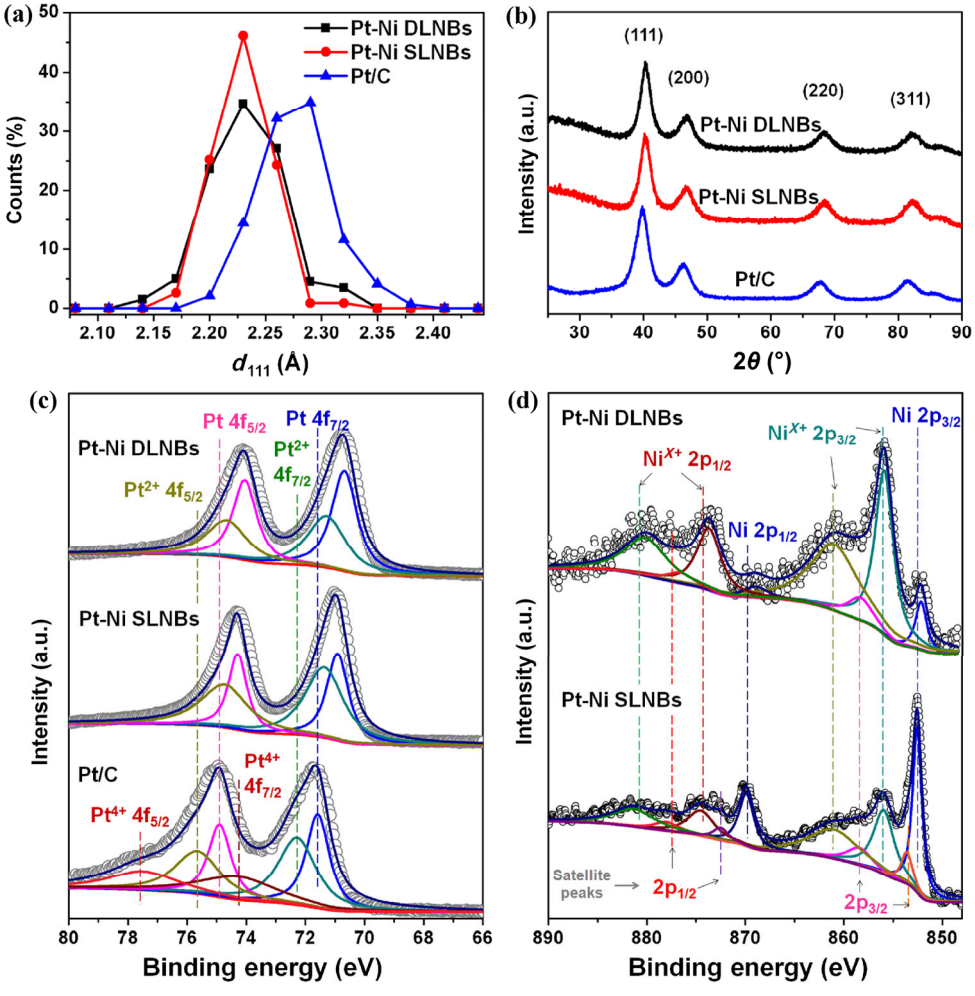

Figure 3 (a) Distribution of d-spacings between the (111) lattice planes of the Pt-Ni DLNBs, SLNBs and the commercial Pt/C catalyst. (b) XRD patterns and (c) XPS spectra of Pt 4f of the three samples. (d) XPS spectra of Ni $2p_{3/2}$ of the Pt-Ni DLNBs and SLNBs.

3.2 Growth mechanism

Using $NaBH_4$ as a reducing agent is an effective strategy to produce hollow Pt-M nanostructures in aqueous solution [28, 31, 36]. In this method, PVP, citric acid, or sodium citrate usually acts as the surfactant or stabilizer. Because the standard reduction potential of the $PtCl_6^{2-}$/Pt pair (E^0 = 0.735 eV vs. SHE) is much higher than that of the Ni^{2+}/Ni pair (E^0 = –0.257 eV vs. SHE), the sequential addition of nickel and platinum precursors led to the formation of hollow, alloyed structures by galvanic replacement and Pt-catalyzed reduction. The reaction equations are described as follows

$$BH_4^- + 4Ni^{2+} + 2H_2O \rightarrow 4Ni\downarrow + BO_2^- + 8H^+ \quad (1)$$

$$2PtCl_6^{2-} + BH_4^- + 2H_2O \rightarrow 2Pt\downarrow + BO_2^- + 12Cl^- + 8H^+ \quad (2)$$

$$2Ni + PtCl_6^{2-} \rightarrow 2Ni^{2+} + Pt + 6Cl^- \quad (3)$$

Our understanding of the Pt-Ni nanobowl formation process is limited because these structures are rarely synthesized. To investigate the growth mechanism, products at different reaction times were extracted and characterized by SEM and TEM. Based on our most recent work [31], the Ni-based particles reduced by $NaBH_4$ in aqueous solution are Ni-B compounds. These Ni-B compounds have an amorphous structure and contain metallic and oxidized Ni species. Furthermore, these Ni-B compounds are easily corroded and dissolved by galvanic replacement reactions of Ni and $PtCl_6^{2-}$ and the corrosion effects of Ni by Cl ions. Based on these results and considering the violent reaction in the first several minutes, samples were

extracted 5, 20, and 60 min after the complete addition of the K_2PtCl_6 solution. Representative SEM images are shown in Fig. 4.

For the Pt-Ni DLNBs, there are no obvious differences in the SEM images between the spheres extracted at 5 and 20 min. However, when characterized by TEM, a dark shell was observed in the sample extracted at 20 min, as shown in Fig. 4(b). This ring is attributed to the dissolution of Ni-B compounds and the deposition of Pt atoms on the surfaces of the growing particles. An important change also occurred at 20 min; that is, the concave structure formed, as shown in the SEM image (Fig. 4(b)). More details are revealed in the TEM image (Fig. 5(c)), where the rough surface and residual Ni-B compounds in the cavity can clearly be distinguished. This observation is different from those of our previous report [29] concerning the formation of bowl-like Pt-Ni structures on the addition of sodium citrate. Generally, bowl-like structures are produced when bowl-like templates or non-equilibrium stress are applied [37, 38]. In this study, spherical particles were the templates and thus, non-equilibrium stress and unstable shells resulted in the concave shape. After 40 min, most spheres had become bowl-like structures, and after reaction for another 80 min, nearly 100% of the structures were nanobowls. Interestingly, the morphology change was accompanied by a decrease in size from 282 nm at 5 min to 256 nm at 120 min. Such a decrease confirms the instability of the spherical shells and was attributed to the compression of the loose structure, which results in a more stable structure.

For the Pt-Ni SLNBs, the growth process can be clearly monitored in the SEM images. At 5 min, as shown in Fig. 4(d), some nanoparticles with bright contrast appeared on the surface of the initial Ni-B compounds, indicating the co-reduction of Pt and Ni. Then, at 20 min, the size of the Ni-B particles decreased significantly and the nanoparticles grew into dome-like structures (Fig. 4(e)). The consumption of the Ni-B compounds and the formation of the dome-like structures can be attributed to the galvanic replacement between $PtCl_6^{2-}$ and Ni, the steric blocking effect of PVP, Ostwald ripening, and the Pt-catalyzed reduction of Ni. The change in shape of most particles from spherical to bowl-like structures occurred at 60 min, as shown in Fig. 4(f).

Generally, surfactants or capping agents have a significant influence on the shape of nanocrystals and the growth of three-dimensional nanostructures [39, 40]. In our protocol, long-chained PVP and ionic citrate

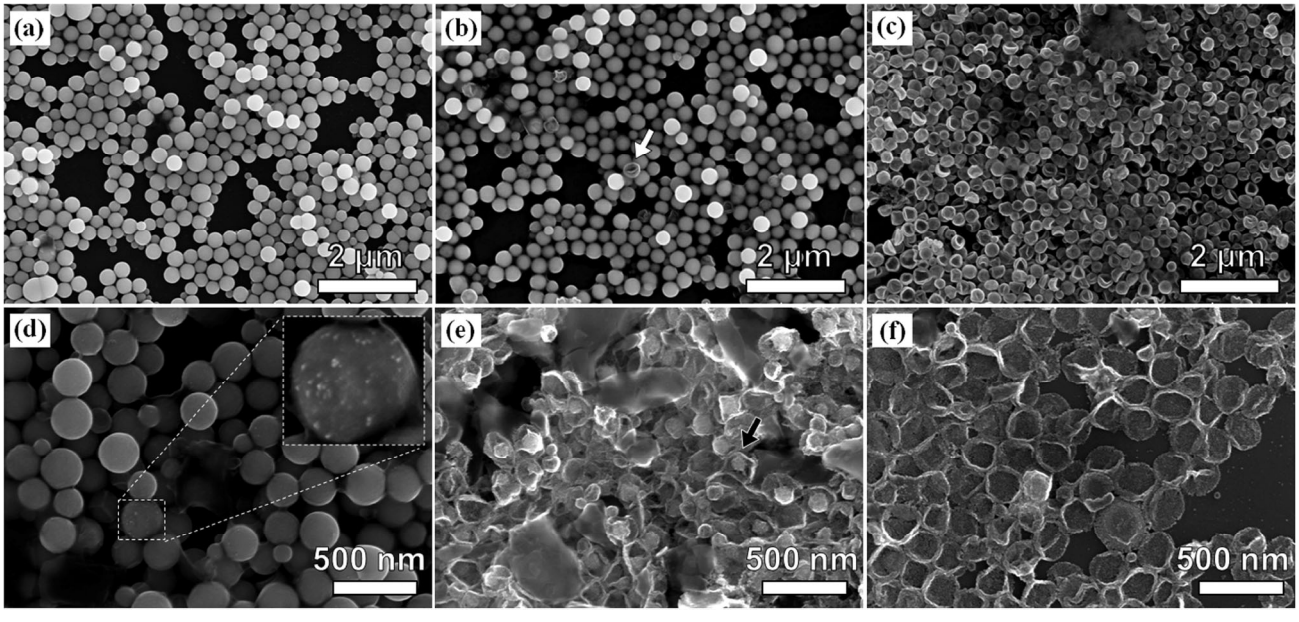

Figure 4 SEM characterization of the morphology evolution of the Pt-Ni ((a)–(c)) DLNBs and ((d)–(f)) SLNBs. The products were obtained at ((a) and (d)) 5 min, ((b) and (e)) 20 min and ((c) and (f)) 60 min after adding K_2PtCl_6. The white arrow in (b) indicates a bowl-like particle. The inserted image in (d) shows some nanoparticles with bright contrast on the surface of the initial Ni-B compounds. The black arrow in (e) indicates a typical intermediate with spherical and dome-like morphology.

both played a critical role in forming the bowl-like structures. When no PVP or sodium citrate was added, a floc-like nanostructure was obtained, and a typical SEM image is shown in Fig. S3(a) (in the ESM). However, when either sodium citrate (5 mg) or PVP (50 mg) was added, some bowl-like structures were formed, as shown in Figs. S3(b) and S3(c) (in the ESM). In our previous work [29], vigorous stirring at a speed of 2,000 rpm was found to be the determining factor for achieving double-layered nanobowls, while decreasing the speed led to fewer nanobowls and more nanospheres. In addition, PVP exhibited an excellent spatial steric effect, stabilizing the bowl-like assemblies of nanoparticles and achieving well-distributed sizes. In this work, the stirring speed was 600 rpm; consequently, the products were of poor quality regarding their morphologies, even after the addition of a larger quantity of PVP (200 mg) (Fig. S3(d) in the ESM). In contrast, adding sodium citrate led to the formation of well-defined nanobowls, but these were formed in low yield, possibly owing to the lack of a proper stabilizing agent. This problem could be solved by adding a more suitable amount of PVP, resulting in the formation of well-defined nanobowls in high yield, as shown in Fig. 1. The size distributions were controlled by the amount of PVP. For example, on adding 5 mg of PVP to prepare the Pt-Ni DLNBs, uneven sizes were obtained, as shown in Fig. S4(a) (in the ESM). Interestingly, the morphologies of the products synthesized by using sodium citrate or PVP were quite different, as shown in Fig. S3 (in the ESM). Using sodium citrate, the formed bowls have sharp brims, whereas, using PVP, they were blunt, demonstrating the different effects of these agents on the bowl-like structures. We found that sodium citrate had a greater impact on the final morphologies than PVP. Previously, citrate has been used to control the growth of Ag and Pt nanostructures because the citrate carboxyl group absorbs to specific crystal faces or sites [41, 42]. Adding 5 mg of sodium citrate resulted in such a blocking effect, leading to the formation of a porous and unstable shell in the DLNBs; this unstable shell was prone to become concave on application of uneven stress, such as that applied in vigorously stirred water. Adding more sodium citrate (15 mg) led to greater citrate adsorption on the surfaces of the nanocrystals, and consequently, these nanocrystals did not form an entirely spherical shell. Instead, Pt-catalyzed reduction promoted growth from specific sites on the surface, forming porous dome-like shells. Meanwhile, galvanic replacement reactions consumed the Ni-B compounds and produced Pt clusters. Ostwald ripening led to the gradual release of Pt from these clusters, which was then deposited on the rapidly growing dome-like shells. In addition, hydrolysis of sodium citrate provided an alkaline environment, which slowed the reduction rate and was beneficial for the adsorption of citrate during the reaction [43]. The reduction rate was determined from the rate of color change of the solution after $NaBH_4$ addition. As shown in Fig. S5 (in the ESM), more sodium citrate led to a slower rate and, thus, a slower reduction rate. In addition, increasing the amount of reactants or the temperature promoted the reaction kinetics, and the solution rapidly became black, eventually leading to the hollow spherical structures shown in Figs. S4(b) and S4(c) (in the ESM).

A schematic illustration of these processes is shown in Scheme 1. Both samples underwent the generation of Ni-B nanospheres due to the reduction effect of $NaBH_4$. Then, after the K_2PtCl_6 solution was injected, a complete shell of Pt-Ni alloy was gradually formed for the DLNB growth, while growth from specific sites on the surface occurred for the SLNBs. During co-reduction, the spherical DLNB structures gradually turned into bowl-like structure with residual Ni-B compounds in the cavities. For the SLNBs, the pre-formed Pt-Ni nanocrystals continued to grow, forming

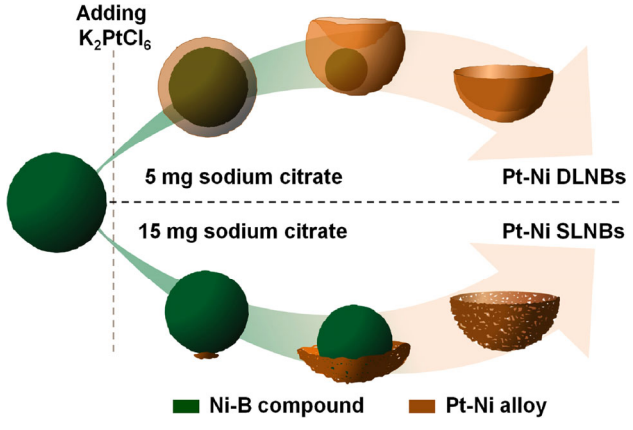

Scheme 1 Schematic illustration of the formation of the Pt-Ni DLNBs and SLNBs.

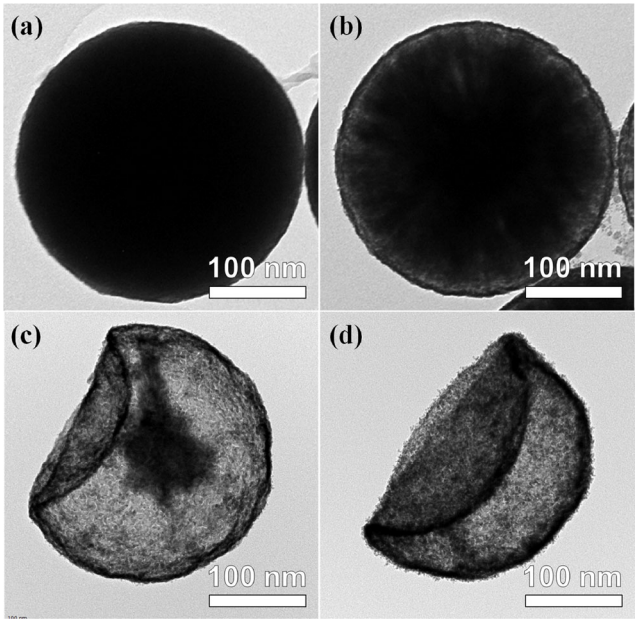

Figure 5 TEM characterization of the evolution of the Pt-Ni DLNBs. The products were obtained at (a) 5, ((b), (c)) 20, and (d) 60 min after adding K_2PtCl_6.

porous, dome-like structures. Once the Ni-B compounds and $NaBH_4$ had been consumed, porous double- and single-layered nanobowls were formed.

In addition to the Pt-Ni nanobowls, this strategy could be modified to prepare other bowl-like metallic nanostructures. For example, Au-Ni double-layered nanobowls were successfully synthesized, as presented in Fig. S4(d) (in the ESM). However, further work is required to investigate their structural and optical features.

3.3 Electrocatalytic properties of the Pt-Ni DLNBs and SLNBs

During the past few decades, direct methanol fuel cells (DMFCs) have become regarded as promising portable power sources because methanol has a high energy density (6,100 $Wh{\cdot}kg^{-1}$) and fast anodic oxidation rates [44–46]. Here, the electrocatalytic oxidation of methanol was conducted using the as-prepared nanobowls and a commercial Pt/C catalyst to evaluate their catalytic performance for use in DMFCs. The ECSAs of the materials were calculated using Eq. (4).

$$\mathrm{ECSA} = Q_m/Q_H \quad (4)$$

Where Q_m is the charge normalized to the loading amount of Pt and calculated from the hydrogen desorption region in the cyclic voltammograms (CVs) in Fig. 6(a) after deduction of the double-layer region, and Q_H is the charge of the monolayer adsorption of hydrogen on the Pt surface (Q_H = 0.21 $mC{\cdot}cm^{-1}$). The ECSAs of Pt-Ni DLNBs and SLNBs were 61.2 and 65.9 $m^2{\cdot}g_{Pt}^{-1}$, respectively, and that of the commercial Pt/C catalyst was 67.9 $m^2{\cdot}g_{Pt}^{-1}$. The as-prepared samples exhibited comparable ECSAs relative to that of the Pt/C catalyst, which arises from their porous structures and alloyed composition. The CVs in methanol solution of the three catalysts measured at 20 ± 1 °C are shown plotted as the mass-specific current density in Fig. 6(b) and area-specific current density in Fig. 6(c). In the forward scan, the Pt-Ni DLNBs and SLNBs showed excellent methanol oxidation mass activities of 646 and 549 $mA{\cdot}mg_{Pt}^{-1}$, respectively, which are about 2.9 and 2.5 times higher, respectively, than that of the Pt/C catalyst (222 $mA{\cdot}mg_{Pt}^{-1}$). The corresponding specific activities are 1.06 $mA{\cdot}cm^{-2}$ for the DLNBs and 0.83 $mA{\cdot}cm^{-2}$ for the SLNBs, 3.2 and 2.5 times higher than that of Pt/C (0.33 $mA{\cdot}cm^{-2}$), respectively. The enhanced specific activity for the MOR can be explained by electronic effects and a bifunctional mechanism. Concerning the electronic effects, the integration of other elements into Pt modifies the electronic structure, causing a shift in the d-band center, which is beneficial in weakening the Pt-CO bond strength and promoting the desorption of carbonaceous intermediates [11]. For the as-prepared Pt-Ni nanobowls, the modification of the electronic structure was confirmed by the negative shifts of Pt $4f_{7/2}$ biding energies (–0.9 eV for DLNBs and –0.7 eV for SLNBs). According to recent work [9, 34, 47], these negative shifts improve the electrocatalytic performance of Pt-based nanomaterials for methanol oxidation. Meanwhile, in the bifunctional mechanism, Ni-based oxides or hydroxides present on the surfaces offer oxygen-containing species that promote the oxidation of carbonaceous intermediates and reproduce the Pt active sites [12]. In this work, the superior activity of DLNBs over SLNBs was ascribed to their higher oxidized Ni content. The ratio of the forward (I_f) and backward (I_b) peak currents is related to the tolerance of a catalyst to the carbonaceous intermediates generated during the electrooxidation of CH_3OH. A higher I_f/I_b ratio indicates better

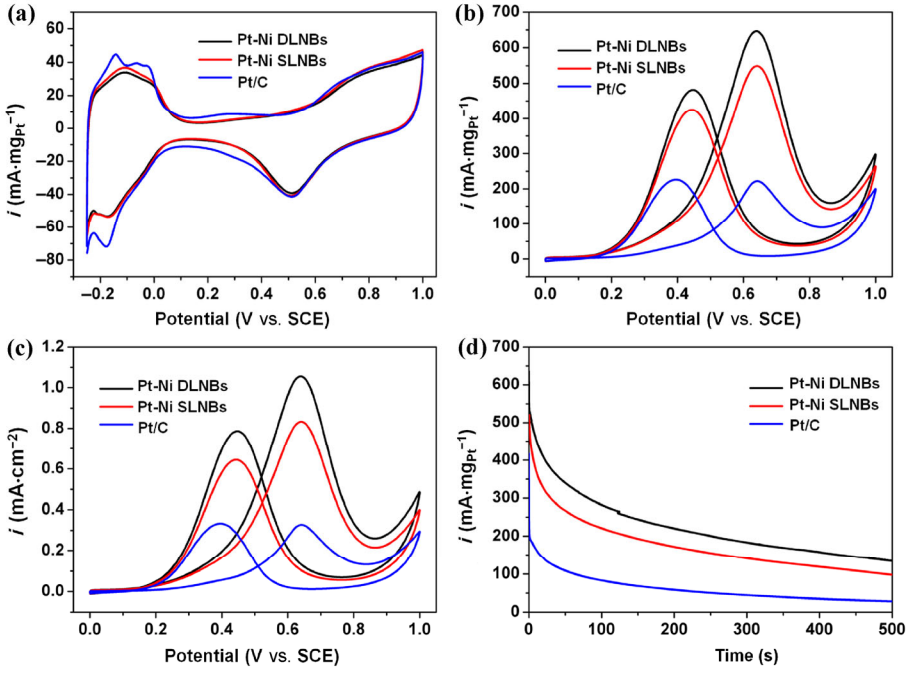

Figure 6 Electrochemical measurements of the Pt-Ni DLNBs, SLNBs, and the commercial Pt/C catalyst at 20 ± 1 ˚C. (a) CV curves in 0.5 M H_2SO_4 solution at a scan rate of 50 mV·s^{-1}. (b) Mass-normalized and (c) ECSA-normalized CV curves in N_2-saturated 0.5 M H_2SO_4 and 1 M methanol solution, scan rate: 50 mV·s^{-1}. (d) CA curves at 0.6 V in 0.5 M H_2SO_4 and 1 M methanol solution.

decomposition of CH_3OH to CO_2 and H_2O and fewer residual intermediates absorbed on the surface of catalyst. In this work, the value of I_f/I_b was about 1.34 for the Pt-Ni DLNBs and 1.29 for the Pt-Ni SLNBs, while that of the Pt/C catalyst was about 0.98. The results indicate that the PtNi nanobowls are more tolerant to poisoning than the commercial Pt/C catalyst. The stability of the catalysts was tested by chronoamperometry (CA) at 0.6 V for 500 s (Fig. 6(d)). Both Pt-Ni nanobowl were more stable than that of the commercial Pt/C catalyst, which might be attributed to the hollow porous structure that prevents aggregation. The electrochemical durabilities of the as-synthesized nanobowls were evaluated by prolonged cycling in 0.5 M H_2SO_4 at a scan rate of 50 mV·s^{-1}. As demonstrated in Fig. S6 (in the ESM), the CV measurements showed a ECSA loss of 24.1% for the Pt-Ni DLNBs, 66.4% for the Pt-Ni SLNBs, and 68.3% for the Pt/C catalyst after 500 potential cycles, demonstrating the significantly better durability of the DLNBs and the slightly better durability of the SLNBs compared to that of the Pt/C catalyst. The morphologies of the three samples after durability tests were characterized by TEM (Fig. S7 in the ESM). All catalysts underwent Ostwald ripening. Aside from having smoother surfaces after electrochemical reaction, the Pt-Ni DLNBs maintained their hollow and concave structures well, as shown in Fig. S7(a) (in the ESM). The Pt-Ni SLNBs suffered from some shape changes but retained their porous structure well, as shown in Fig. S7(b) (in the ESM). As for the Pt/C catalyst, serious aggregation and ripening processes can be clearly seen in the SEM image (Fig. S7(d) in the ESM) compared with images of the catalyst before the reaction shown in Fig. S7(c) (in the ESM). These results demonstrate that the Pt-Ni nanobowls, especially the DLNBs, are more structurally durable than the Pt/C catalyst. In summary, the Pt-Ni nanobowls exhibited enhanced electrocatalytic performance for methanol oxidation and are promising catalysts with applications in DMFCs.

4 Conclusions

Layer-controlled syntheses of Pt-Ni porous nanobowls were carried out in aqueous solutions at ambient temperature. Their shells were constructed of alloyed Pt-Ni nanocrystals and small amounts of Ni compounds.

The double-layered nanobowls contained a greater amount of oxidized Ni species than the single- layered ones. A formation mechanism, based on the adsorption of citrate, was proposed to explain the different growth patterns. The double- and single-layered Pt-Ni nanobowls exhibited 2.9 and 2.5 times higher mass activity, respectively, and better stability than those of the commercial Pt/C catalyst for catalyzing the methanol oxidation reaction. The enhanced catalytic performance was attributed to electronic effects, the bifunctional mechanism, and the hollow, porous structures of the nanobowls. It is expected that these Pt-Ni nanobowls will be promising catalysts for DMFCs and other sustainable energy technologies. Furthermore, our work provides a strategy to prepare other bowl- like metallic advanced energy nanomaterials.

Acknowledgements

This work was supported by the National Natural Science Foundation of China (Nos. 51371015 and 51331002), the Beijing Natural Science Foundation (No. 2142018) and the Fundamental Research Funds for the Central Universities (No. FRF-BR-15-009B).

Electronic Supplementary Material: Supplementary material (EDS results, additional XPS results, additional SEM and TEM images) is available in the online version of this article at http://dx.doi.org/10.1007/s12274-016-1277-5.

References

[1] Chen, A. C.; Holt-Hindle, P. Platinum-based nanostructured materials: Synthesis, properties, and applications. *Chem. Rev.* **2010**, *110*, 3767–3804.

[2] Peng, Z. M.; Yang, H. Designer platinum nanoparticles: Control of shape, composition in alloy, nanostructure and electrocatalytic property. *Nano Today* **2009**, *4*, 143–164.

[3] Wang, Y. J.; Zhao, N.; Fang, B. Z.; Li, H.; Bi, X. T.; Wang, H. J. Carbon-supported Pt-based alloy electrocatalysts for the oxygen reduction reaction in polymer electrolyte membrane fuel cells: Particle size, shape, and composition manipulation and their impact to activity. *Chem. Rev.* **2015**, *115*, 3433–3467.

[4] Hansen, T. W.; Delariva, A. T.; Challa, S. R.; Datye, A. K. Sintering of catalytic nanoparticles: Particle migration or ostwald ripening? *Acc. Chem. Res.* **2013**, *46*, 1720–1730.

[5] Huang, H. J.; Wang, X. Recent progress on carbon-based support materials for electrocatalysts of direct methanol fuel cells. *J. Mater. Chem. A* **2014**, *2*, 6266–6291.

[6] Xu, Y.; Zhang, B. Recent advances in porous Pt-based nanostructures: Synthesis and electrochemical applications. *Chem. Soc. Rev.* **2014**, *43*, 2439–2450.

[7] Cao, X.; Han, Y.; Gao, C. Z.; Xu, Y.; Huang, X. M.; Willander, M.; Wang, N. Highly catalytic active PtNiCu nanochains for hydrogen evolution reaction. *Nano Energy* **2014**, *9*, 301–308.

[8] Nosheen, F.; Zhang, Z. C.; Xiang, G. L.; Xu, B.; Yang, Y.; Saleem, F.; Xu, X. B.; Zhang, J. C.; Wang, X. Three-dimensional hierarchical Pt-Cu superstructures. *Nano Res.* **2015**, *8*, 832–838.

[9] Zhang, J. F.; Li, K. D.; Zhang, B. Synthesis of dendritic Pt-Ni-P alloy nanoparticles with enhanced electrocatalytic properties. *Chem. Commun.* **2015**, *51*, 12012–12015.

[10] Jung, N.; Chung, D. Y.; Ryu, J.; Yoo, S. J.; Sung, Y.-E. Pt-based nanoarchitecture and catalyst design for fuel cell applications. *Nano Today* **2014**, *9*, 433–456.

[11] Hammer, B.; Morikawa, Y.; Nørskov, J. K. CO chemisorption at metal surfaces and overlayers. *Phys. Rev. Lett.* **1996**, *76*, 2141–2144.

[12] Kua, J.; Goddard, W. A. Oxidation of methanol on 2nd and 3rd row group VIII transition metals (Pt, Ir, Os, Pd, Rh, and Ru): Application to direct methanol fuel cells. *J. Am. Chem. Soc.* **1999**, *121*, 10928–10941.

[13] Chen, C.; Kang, Y. J.; Huo, Z. Y.; Zhu, Z. W.; Huang, W. Y.; Xin, H. L.; Snyder, J. D.; Li, D. G.; Herron, J. A.; Mavrikakis, M. et al. Highly crystalline multimetallic nanoframes with three-dimensional electrocatalytic surfaces. *Science* **2014**, *343*, 1339–1343.

[14] Zhang, H.; Jin, M. S.; Liu, H. Y.; Wang, J. G.; Kim, M. J.; Yang, D. R.; Xie, Z. X.; Liu, J. Y.; Xia, Y. N. Facile synthesis of Pd-Pt alloy nanocages and their enhanced performance for preferential oxidation of CO in excess hydrogen. *ACS Nano* **2011**, *5*, 8212–8222.

[15] Song, Y. J.; Garcia, R. M.; Dorin, R. M.; Wang, H. R.; Qiu, Y.; Shelnutt, J. A. Synthesis of platinum nanocages by using liposomes containing photocatalyst molecules. *Angew. Chem., Int. Ed.* **2006**, *45*, 8126–8130.

[16] Dubau, L.; Asset, T.; Chattot, R.; Bonnaud, C.; Vanpeene, V.; Nelayah, J.; Maillard, F. Tuning the performance and the stability of porous hollow PtNi/C nanostructures for the oxygen reduction reaction. *ACS Catal.* **2015**, *5*, 5333–5341.

[17] Mahmoud, M. A.; Narayanan, R.; El-Sayed, M. A. Enhancing colloidal metallic nanocatalysis: Sharp edges and corners for solid nanoparticles and cage effect for hollow ones. *Acc. Chem. Res.* **2013**, *46*, 1795–1805.

[18] Garcia, R. M.; Song, Y. J.; Dorin, R. M.; Wang, H. R.; Li, P.; Qiu, Y.; van Swol, F.; Shelnutt, J. A. Light-driven synthesis of hollow platinum nanospheres. *Chem. Commun.* **2008**, 2535–2537.

[19] Cui, C.-H.; Li, H.-H.; Yu, S.-H. Large scale restructuring of porous Pt-Ni nanoparticle tubes for methanol oxidation: A highly reactive, stable, and restorable fuel cell catalyst. *Chem. Sci.* **2011**, *2*, 1611–1614.

[20] Cai, K.; Lv, Z. C.; Chen, K.; Huang, L.; Wang, J.; Shao, F.; Wang, Y. J.; Han, H. Y. Aqueous synthesis of porous platinum nanotubes at room temperature and their intrinsic peroxidase-like activity. *Chem. Commun.* **2013**, *49*, 6024–6026.

[21] Alia, S. M.; Zhang, G.; Kisailus, D.; Li, D. S.; Gu, S.; Jensen, K.; Yan, Y. S. Porous platinum nanotubes for oxygen reduction and methanol oxidation reactions. *Adv. Funct. Mater.* **2010**, *20*, 3742–3746.

[22] Xia, B. Y.; Wu, H. B.; Wang, X.; Lou, X. W. One-pot synthesis of cubic $PtCu_3$ nanocages with enhanced electrocatalytic activity for the methanol oxidation reaction. *J. Am. Chem. Soc.* **2012**, *134*, 13934–13937.

[23] Nosheen, F.; Zhang, Z. C.; Zhuang, J.; Wang, X. One-pot fabrication of single-crystalline octahedral Pt-Cu nanoframes and their enhanced electrocatalytic activity. *Nanoscale* **2013**, *5*, 3660–3663.

[24] Zhang, Z. C.; Yang, Y.; Nosheen, F.; Wang, P. P.; Zhang, J. C.; Zhuang, J.; Wang, X. Fine tuning of the structure of Pt-Cu alloy nanocrystals by glycine-mediated sequential reduction kinetics. *Small* **2013**, *9*, 3063–3069.

[25] Wu, Y. E.; Wang, D. S.; Zhou, G.; Yu, R.; Chen, C.; Li, Y. D. Sophisticated construction of Au islands on Pt-Ni: An ideal trimetallic nanoframe catalyst. *J. Am. Chem. Soc.* **2014**, *136*, 11594–11597.

[26] Oh, A.; Baik, H.; Choi, D. S.; Cheon, J. Y.; Kim, B.; Kim, H.; Kwon, S. J.; Joo, S. H.; Jung, Y.; Lee, K. Skeletal octahedral nanoframe with cartesian coordinates via geometrically precise nanoscale phase segregation in a Pt@Ni core–shell nanocrystal. *ACS Nano* **2015**, *9*, 2856–2867.

[27] Wang, L.; Yamauchi, Y. Metallic nanocages: Synthesis of bimetallic Pt-Pd hollow nanoparticles with dendritic shells by selective chemical etching. *J. Am. Chem. Soc.* **2013**, *135*, 16762–16765.

[28] Sun, Q.; Ren, Z.; Wang, R. M.; Wang, N.; Cao, X. Platinum catalyzed growth of NiPt hollow spheres with an ultrathin shell. *J. Mater. Chem.* **2011**, *21*, 1925–1930.

[29] Sun, Q.; Liu, W.; Wang, R. M. Double-layered NiPt nanobowls with ultrathin shell synthesized in water at room temperature. *CrystEngComm* **2012**, *14*, 5151–5154.

[30] Liu, J. L.; Liu, W.; Sun, Q.; Wang, S. G.; Sun, K.; Schwank, J.; Wang, R. M. *In situ* tracing of atom migration in Pt/NiPt hollow spheres during catalysis of CO oxidation. *Chem. Commun.* **2014**, *50*, 1804–1807.

[31] Shan, A. X.; Chen, Z. C.; Li, B. Q.; Chen, C. P.; Wang, R. M. Monodispersed, ultrathin NiPt hollow nanospheres with tunable diameter and composition via a green chemical synthesis. *J. Mater. Chem. A* **2015**, *3*, 1031–1036.

[32] Liu, J. L.; Xia, T. Y.; Wang, S. G.; Yang, G.; Dong, B. W.; Wang, C.; Ma, Q. D.; Sun, Y.; Wang, R. M. Oriented-assembly of hollow FePt nanochains with tunable catalytic and magnetic properties. *Nanoscale* **2016**, *8*, 11432–11440.

[33] Mou, F. Z.; Xu, L. L.; Ma, H. R.; Guan, J. G.; Chen, D. R.; Wang, S. H. Facile preparation of magnetic gamma-Fe_2O_3/TiO_2 janus hollow bowls with efficient visible-light photocatalytic activities by asymmetric shrinkage. *Nanoscale* **2012**, *4*, 4650–4657.

[34] Zhang, G. L.; Huang, C. D.; Qin, R. J.; Shao, Z. C.; An, D.; Zhang, W.; Wang, Y. X. Uniform Pd–Pt alloy nanoparticles supported on graphite nanoplatelets with high electrocatalytic activity towards methanol oxidation. *J. Mater. Chem. A* **2015**, *3*, 5204–5211.

[35] Biesinger, M. C.; Payne, B. P.; Grosvenor, A. P.; Lau, L. W. M.; Gerson, A. R.; Smart, R. S. C. Resolving surface chemical states in XPS analysis of first row transition metals, oxides and hydroxides: Cr, Mn, Fe, Co and Ni. *Appl. Surf. Sci.* **2011**, *257*, 2717–2730.

[36] Liang, H. P.; Zhang, H. M.; Hu, J. S.; Guo, Y. G.; Wan, L. J.; Bai, C. L. Pt hollow nanospheres: Facile synthesis and enhanced electrocatalysts. *Angew. Chem.* **2004**, *43*, 1540–1543.

[37] Li, X. L.; Zhang, Y. Z.; Shen, Z. X.; Fan, H. J. Highly ordered arrays of particle-in-bowl plasmonic nanostructures for surface-enhanced raman scattering. *Small* **2012**, *8*, 2548–2554.

[38] Liang, J.; Hu, H.; Park, H.; Xiao, C. H.; Ding, S. J.; Paik, U.; Lou, X. W. Construction of hybrid bowl-like structures by anchoring NiO nanosheets on flat carbon hollow particles with enhanced lithium storage properties. *Energy Environ. Sci.* **2015**, *8*, 1707–1711.

[39] Duan, S. B.; Wang, R. M. Au/$Ni_{12}P_5$ core/shell nanocrystals from bimetallic heterostructures: *In situ* synthesis, evolution and supercapacitor properties. *NPG Asia Mater.* **2014**, *6*, e122.

[40] Xie, J. P.; Zhang, Q. B.; Zhou, W. J.; Lee, J. Y.; Wang, D. I. C. Template-free synthesis of porous platinum networks of different morphologies. *Langmuir* **2009**, *25*, 6454–6459.

[41] Kilin, D. S.; Prezhdo, O. V.; Xia, Y. N. Shape-controlled synthesis of silver nanoparticles: *Ab initio* study of preferential surface coordination with citric acid. *Chem. Phys. Lett.* **2008**, *458*, 113–116.

[42] Bai, Z. Y.; Yang, L.; Zhang, J. S.; Li, L.; Hu, C. G.; Lv, J.; Guo, Y. M. High-efficiency carbon-supported platinum catalysts stabilized with sodium citrate for methanol oxidation. *J. Power Sources* **2010**, *195*, 2653–2658.

[43] Henglein, A.; Giersig, M. Reduction of Pt(II) by H_2: Effects of citrate and NaOH and reaction mechanism. *J. Phys. Chem. B* **2000**, *104*, 6767–6772.

[44] Zhao, X.; Yin, M.; Ma, L.; Liang, L.; Liu, C. P.; Liao, J. H.; Lu, T. H.; Xing, W. Recent advances in catalysts for direct methanol fuel cells. *Energy Environ. Sci.* **2011**, *4*, 2736–2753.

[45] Kimiaie, N.; Wedlich, K.; Hehemann, M.; Lambertz, R.; Müller, M.; Korte, C.; Stolten, D. Results of a 20000 h lifetime test of a 7 kW direct methanol fuel cell (DMFC) hybrid system – degradation of the DMFC stack and the energy storage. *Energy Environ. Sci.* **2014**, *7*, 3013–3025.

[46] Wang, N.; Xu, Y.; Han, Y.; Gao, C. Z.; Cao, X. Mesoporous Pd@M (M = Pt, Au) microrods as excellent electrocatalysts for methanol oxidation. *Nano Energy* **2015**, *17*, 111–119.

[47] Lu, Y. Z.; Jiang, Y. Y.; Chen, W. Graphene nanosheet-tailored PtPd concave nanocubes with enhanced electrocatalytic activity and durability for methanol oxidation. *Nanoscale* **2014**, *6*, 3309–3315.